

Emergence of the modern global monsoon from the Pangaea megamonsoon set by palaeogeography

Received: 28 September 2022

Accepted: 8 September 2023

Published online: 19 October 2023

Yongyun Hu¹✉, Xiang Li¹, William R. Boos², Jiaqi Guo¹, Jiawenjing Lan¹, Qifan Lin¹, Jing Han¹, Jian Zhang¹, Xiujuan Bao¹, Shuai Yuan¹, Qiang Wei¹, Yonggang Liu¹, Jun Yang¹, Ji Nie¹ & Zhengtang Guo¹✉

 Check for updates

Geologic evidence and palaeoclimate simulations have indicated the existence of an extensive, interconnected megamonsoon system over the Pangaea supercontinent. However, the ways in which subsequent continental break-up about 180 million years ago and reassembly in the Cenozoic, as well as large global climatic fluctuations, influenced the transition to the modern global monsoon system are uncertain. Here we use a large set of simulations of global climate every 10 million years over the past 250 million years to show that the monsoon system evolved in three stages due to changes in palaeogeography: a spatially extensive land monsoon with weak precipitation in the Triassic period (>170 Ma), a smaller land monsoon with intense precipitation in the Cretaceous period (170–70 Ma) and a return to a broader, weaker monsoon in the Cenozoic era (<70 Ma). It is found that global-mean temperature variations have little impact on global land-monsoon area and intensity over tectonic timescales. Applying an analysis of atmospheric energetics, we show that these variations of the global land monsoon are governed by continental area, latitudinal location and fragmentation.

The monsoon system is the dominant seasonal mode of the global hydrological cycle^{1–3}, influencing the livelihoods of billions of people at present⁴. However, understanding monsoon dynamics and projecting future long-term changes in monsoon rainfall remain great challenges. The study of deep-time monsoons can help improve our understanding of the modern monsoon system and its variations with global climate^{3,4}.

Monsoons are driven by land–sea contrasts in energy sources, with off-equatorial tropical continents transferring more energy from summer sunlight into the overlying atmosphere than do adjacent ocean regions⁵. Over tectonic timescales, continents undergo the Wilson cycle, with supercontinent break-up and the reassembly of

fragmented continents⁶. Pangaea is the most recent supercontinent, estimated to have broken up about 180 million years ago (Ma). Highly fragmented continents were most widespread in the late Cretaceous period and reassembled in the Cenozoic era. The Wilson cycle also involves changes in continental area, latitudinal location and orography, all of which would be expected to alter land–sea heating contrasts and consequently the monsoon system^{7–9}.

Studies of deep-time monsoons have thus far focused mainly on two geochronologic units: the Triassic period with its Pangaea mega-monsoon^{10–14} and the Cenozoic era with its large concurrent variations in Asian orography and monsoon rainfall^{15–27}. The important question

¹Laboratory for Climate and Ocean–Atmosphere Studies, Department of Atmospheric and Oceanic Sciences, School of Physics, Peking University, Beijing, China. ²Department of Earth and Planetary Science, University of California, Berkeley, Berkeley, CA, USA. ³Key Laboratory of Cenozoic Geology and Environment, Institute of Geology and Geophysics, Chinese Academy of Sciences, Beijing, China. ✉e-mail: yahu@pku.edu.cn; ztguo@mail.igcas.ac.cn

of how the modern monsoon system originated from the Pangaea megamonsoon has not been studied. To our knowledge, only three works focus on the evolution of the global monsoon in deep time. One used coal and evaporite proxies to reconstruct land-monsoon rainfall patterns in the Mesozoic and Cenozoic eras²⁸. The other two simulated the evolution of the Southeast Asian monsoon and the South American and African monsoons from the Cretaceous to the present^{26,27}. They demonstrated that variations of these regional monsoons are controlled mainly by palaeogeographic changes, including widening of the South Atlantic and uplift of mountains.

In this Article, we study the evolution of the monsoon system, in the context of the global monsoon concept, as continents break up and reassemble over the past 250 million years (Myr), focusing on the global land monsoon. The global monsoon is the dominant mode of the annual variation of precipitation and circulation in the global tropics and subtropics^{1–3}. It reflects the coherent variations of regional monsoons in space and time. We give particular attention to variations in land-monsoon area and precipitation intensity, which were not distinguished in previous palaeo-monsoon studies; we will show that these two measures can be anticorrelated, potentially causing confusion in attempts to interpret proxies. Using a fully coupled atmosphere–ocean Earth system model, we perform 26 time-slice simulations of global climate evenly distributed over the past 250 Myr^{29,30}. The simulations are constrained with reconstructions of palaeogeography⁶, global-mean surface temperatures (GMSTs)^{31,32} and linearly increasing solar radiation^{31,32}. The global monsoon domain is defined with the monsoon precipitation index^{1,2} (Methods).

Global monsoon domains across time

The global monsoon changes greatly over the 250 Myr of simulated time, originating with the Pangaea megamonsoon seen in previous simulations^{10,12}, with the Tethys coast dominated by monsoon rainfall (Fig. 1; monsoon domains for each simulation are shown in Extended Data Fig. 1). The monsoon domain then becomes much smaller by 80 Ma, especially in the Northern Hemisphere (NH), as fragmented continents move out of the tropics. However, precipitation over most continental monsoon regions is stronger at 80 Ma than at 240 Ma. Finally, for the pre-industrial simulation (Fig. 1c), monsoon areas become broader again, especially in Asia. The global monsoon domain in Fig. 1c generally resembles that in current observations¹, indicating that the model reasonably simulates the modern global monsoon. Cross-equatorial monsoonal flows are associated with the megamonsoon and the Asian monsoon (Fig. 1a,c). Specifically, the monsoonal flow extends to the extratropical monsoon regions on east coasts in all times (Extended Data Fig. 1). Dry areas are generally located on the western sides of continents, with peak extent near 30° latitude (Fig. 1 and Extended Data Fig. 1), as expected due to the remote drying that atmospheric waves induce west of intense precipitation³³; this monsoon–dry zone pattern remains relatively unchanged across time.

To compare with geological records, we plot locations of coals and land evaporites in Fig. 1 and Extended Data Fig. 1 (ref. 34). Coals are located mainly in rainy regions, such as monsoon domains, the Equator and land regions in the extratropical storm track (roughly 55° off the Equator), while land evaporites are deposited mainly in dry regions. There are some disagreements between evaporites and the simulations. That is, some evaporites are found in monsoon domains. However, as pointed out in early works²⁸, evaporites can be formed in monsoonal regions because of large seasonal variations of precipitation and temperatures. Moreover, there are uncertainties of both evaporite palaeo-locations and ages³⁴ (Methods). The percentage of the global land-monsoon area here is similar to that estimated with the biogenic Si burial rate of deep-sea chert³⁵.

Anticorrelated land-monsoon area and intensity

We now examine how and why the extent of the land-monsoon domain changed over time. Although ocean regions are an integral part of the global

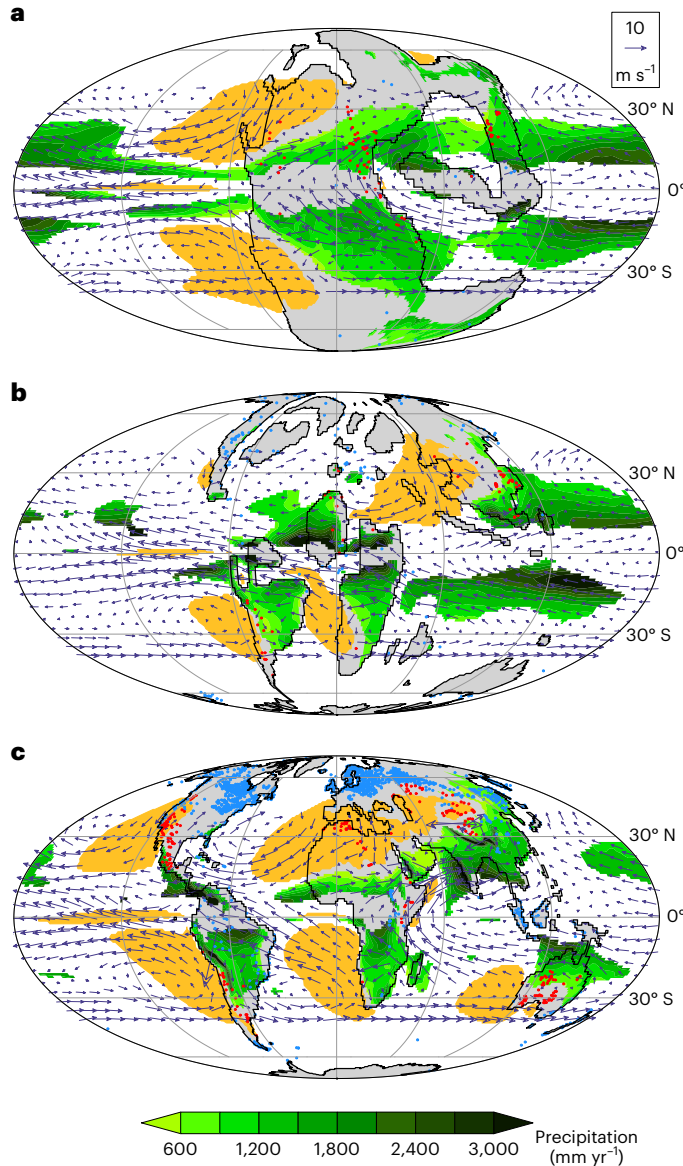


Fig. 1 | Global monsoon domains defined by the monsoon precipitation index^{1,2}. Green shading marks monsoon domains, with the colour representing the annual precipitation amount (colour-bar interval is 300 mm yr^{-1}). Yellow shading denotes dry areas. **a**, 240 Ma. **b**, 80 Ma. **c**, Pre-industrial. Arrows denote 850 hPa winds averaged over June–July–August. Blue and red dots denote coals and land evaporites⁵⁰, respectively.

monsoon system¹, we focus on the global land monsoon because there are more proxies and it is more relevant to modern societal impacts.

Figure 2 shows time series of global land-monsoon area and annual-mean precipitation in the land-monsoon domain over the past 250 Myr. Land-monsoon area was broad from 250 to 180 Ma (solid blue line), spanning about 12% of Earth's surface area, with a maximum value of about 13.6% at 180 Ma. It decreased after 180 Ma, when the Pangaea supercontinent started breaking up and NH continents moved towards higher latitudes. Land-monsoon area became much smaller in the Cretaceous, with the area averaged from the period 130–80 Ma being only half that of 250–180 Ma. The minimum value of 6.2% occurred at 80 Ma, when continents were most dispersed and total continental area was smallest. As continents started reassembling after 80 Ma, land-monsoon area began to increase. The decrease in land-monsoon area after 40 Ma is associated largely with northern Africa moving into the NH subtropical dry zone (Extended Data Fig. 1v–z).

Land-monsoon precipitation intensity is highly anticorrelated with land-monsoon area ($r = -0.87$), being weak before 180 Ma, strong in the Cretaceous around 100 Ma and weak again in the Cenozoic (solid orange line in Fig. 2). Here we define land-monsoon precipitation intensity as the annual-mean precipitation averaged over land-monsoon regions.

A question is whether GMST, which varied more than 12 °C in the past 250 Myr^{31,32}, caused past changes in the global land monsoon. To distinguish the influence of continental configuration from that of GMST, we performed 26 sensitivity simulations with CO₂ concentration fixed at ten times that of the pre-industrial and solar constant fixed at the present value (Methods). The thin dashed lines in Fig. 2 show results from these sensitivity simulations, which nearly overlap the solid lines for most of the 250 Myr. It indicates that changes in GMSTs and CO₂ concentrations have a minor effect on land-monsoon area and precipitation over tectonic timescales, with a typical relative deviation between the control and sensitivity simulations of about 10%. The deviation increases in the later Cenozoic and is largest for land-monsoon precipitation intensity in the pre-industrial (although land-monsoon area deviates little then); here we focus on changes over geological time and simply note that this CO₂-induced increase in monsoon precipitation with modern geography is consistent with previous work³⁶.

Land-monsoon area determined primarily by tropical continental area

The results in Figs. 1 and 2 indicate that land-monsoon area and land-monsoon precipitation intensity are controlled primarily by continental configuration but provide little insight on controlling mechanisms. Given that much tropical land in the modern climate is monsoonal¹⁵, a simple prediction is that land-monsoon area scales with tropical continental area. Tropical continental area (<30° latitude) indeed correlates strongly with simulated land-monsoon area ($r = 0.93$; Fig. 3d). Total continental area, which is not conserved across time, also correlates well with land-monsoon area ($r = 0.82$), but not as strongly as does tropical land area. The fraction of continental area that is monsoonal varies over time, from 37% between 250 and 180 Ma to 23% at 130 Ma (Extended Data Fig. 2). When continents are smaller, more fragmented and located at higher latitudes, such as in the Cretaceous, land-monsoon area is smaller, whereas assembled tropical continents, such as Pangaea and modern Africa–Eurasia, generate a broader land-monsoon area. As shown in Extended Data Fig. 3a, land-monsoon area has high anticorrelation with continental fragmentation ($r = -0.79$).

Although these results are consistent with the hypothesis that land-monsoon area is controlled by tropical land area, the seasonal energy source produced by extratropical land is known to influence the extent of tropical monsoons⁵. This becomes evident from the distribution of net energy input (NEI) through the top and bottom of the atmosphere, which theoretical frameworks treat as a driver of precipitating seasonal-mean tropical circulations such as monsoons^{5,37,38}. The NEI is positive and strong over tropical and subtropical lands in the summer hemisphere (Fig. 3a–c). Its connection to atmospheric circulation can be visualized by taking its inverse Laplacian, yielding an energy flux potential³⁹. Tropical precipitation maxima typically lie near minima of this potential, which at each longitude is known as the energy flux equator (EFE; red curves in Fig. 3a–c); previous studies have shown that the EFE shifts meridionally with tropical rainfall maxima³⁸.

We construct a diagnostic energy-based index for the land-monsoon domain by summing land area lying within an extreme value (the eighth percentile; Methods) of the energy flux potential at each solstice season. This index tracks land-monsoon area well (Fig. 3d; $r = 0.8$); it is a slightly worse predictor than tropical land area, but it complements the tropical land area metric in that it excludes some tropical land and includes some extratropical land. One example of

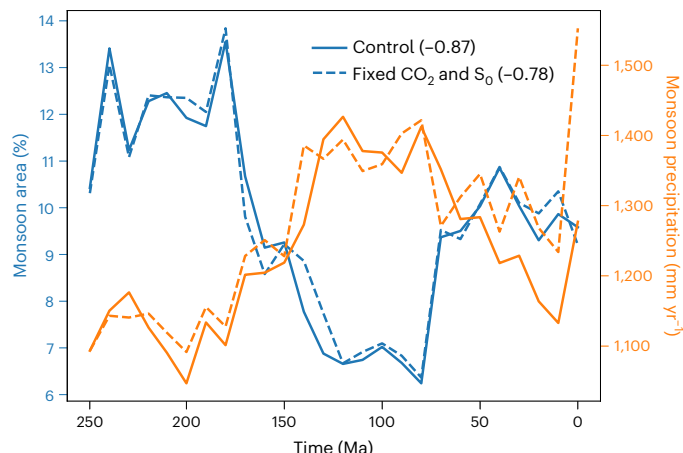


Fig. 2 | Time series of global land-monsoon area and land-monsoon intensity. Solid lines are for control simulations, and thin dashed lines are for sensitivity simulations. Blue lines represent global land-monsoon area as the percentage of Earth's surface area (left axis), and orange lines are annual-mean precipitation averaged over land-monsoon domains (right axis, mm yr⁻¹). Correlation coefficients between land-monsoon area and intensity are labelled at the upper-right corner.

its excursions into the subtropics is at 240 Ma in austral summer, when the EFE and energy flux potential minimum migrate polewards of 30°S over southeastern Pangaea (Fig. 3a, green line). Since extratropical NEI can shift the EFE and energy flux potential within the tropics³⁹, these diagnostics demonstrate the additional importance of extratropical land for shifts of the monsoon domain within the tropics.

Land-monsoon intensity determined mainly by continental fragmentation

We next investigate the variation of land-monsoon intensity. Land-monsoon intensity covaries strongly with convective instability over monsoonal land, as approximated by the relative moist static energy (MSE) averaged over monsoonal land (Fig. 4d; $r = 0.84$). Relative MSE is local surface air MSE minus tropical-mean surface air MSE; it generalizes relative sea surface temperature, which has been influential in understanding variations in tropical cyclone activity^{40,41} and represents the degree to which a given region is warmer and more humid than the tropical mean, and thus convectively unstable. Relative MSE has been shown to explain globally inhomogeneous future changes in monsoons⁴² and variations in monsoon synoptic activity⁴³.

Relative MSE is high over near-equatorial land and low on the western side of off-equatorial tropical continents (Fig. 4a–c; shading shows relative MSE in the land-monsoon domain, while colour contours show it globally). This is because stationary Rossby waves propagate westwards from precipitating regions³³. These stationary waves consist of cyclonic low-level gyres that, on their western sides, transport colder and drier (lower MSE) air into the tropics (magenta vectors in Fig. 4a–c; annual-mean values are shown here for simplicity and brevity, but Extended Data Fig. 5 shows boreal and austral summer distributions). It was shown that this advective transport reduces relative MSE on the poleward and western edges of monsoon domains (shading in Fig. 4a–c) and reduces monsoon intensity by importing dry air into the monsoon region⁴². Linear models yield zonal scales of several equatorial Rossby deformation radii (each radius being about 1,000 km) for these Rossby gyres, so fragmented continents of the Cretaceous are too small to extend into the dry part of these gyres, except over Eurasia, the results in the land-monsoon domain having averagely higher relative MSE. Excluding the extratropical monsoon domain from the average of relative MSE does not affect this result (Extended Data Fig. 4). By contrast, Pangaea and modern Africa–Eurasia are large

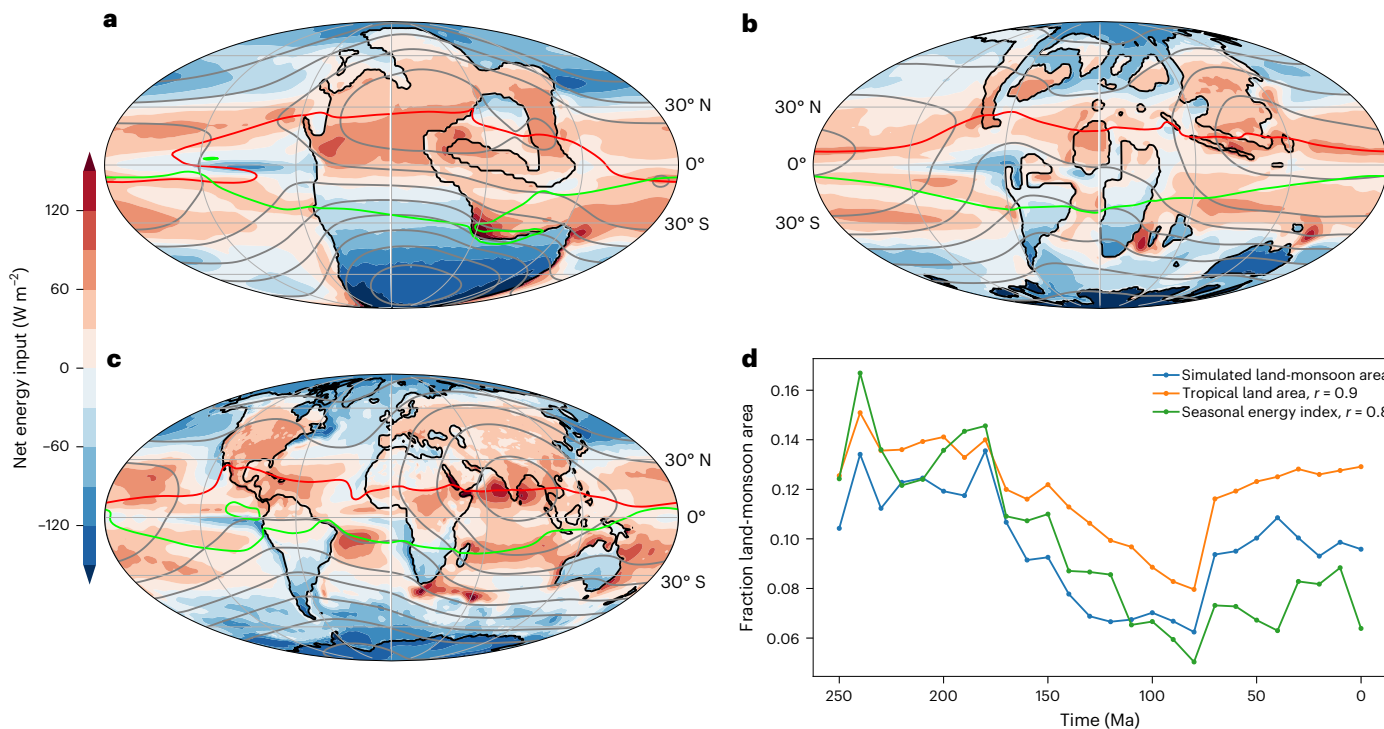


Fig. 3 | Energetics governing the influence of continental configuration on monsoon area. **a–c**, Boreal summer net energy input to the atmosphere (colour shading, W m^{-2}), the energy flux potential (grey contours, contour interval 0.2 PW, with minima located in the tropics and maxima near the poles) and the EFE (red line) at 240 Ma (**a**), 80 Ma (**b**) and pre-industrial (**c**). The austral summer EFE is also shown in green, for comparison with the monsoon domains in Fig. 1. **d**,

Time series of the fraction of global surface area occupied by the land-monsoon domain (blue curve), the energy-based index for this land-monsoon area (green) and the fraction of global surface area occupied by tropical land (orange). Correlation coefficients between the simulated land-monsoon area and each other quantity are noted in the legend. Panel **d** shows results for the full year, while **a–c** use boreal summer as an illustrative example.

enough to have substantial fractions of continents, with their larger monsoon domains, extending into the dry zone of the Rossby gyres, reducing the mean land-monsoon precipitation.

The hypothesis that land-monsoon intensity is driven by continental fragmentation, through the mediating mechanism of circulation-driven relative MSE, is supported by the strong correlation between land-monsoon intensity and continental fragmentation ($r = 0.80$; Fig. 4d and Extended Data Fig. 3). There is a large deviation between fragmentation and land-monsoon intensity over 130–80 Ma, but the relative MSE follows intensity in that period, supporting its importance as a controlling mechanism.

To further address the role of continental configuration in determining land monsoons, we perform eight idealized simulations. Land-monsoon area decreases as the idealized supercontinent is moved from the tropics to extratropics (Extended Data Fig. 6, left panels). Land monsoon almost disappears when the supercontinent is located north of 30°N (Extended Data Fig. 6g). A humid, high-MSE region lies over the southern part of the continent when the continent is positioned in the tropics, with a low-MSE desert region to the north/northwest (Extended Data Fig. 7), as expected from past work^{42,44}. The right panels show that larger continents have a broader land-monsoon area. Extended Data Fig. 8 shows that smaller continents have stronger land-monsoon precipitation, except when southern continental boundaries are located at the Equator.

The preceding results suggest that the Pangaea megamonsoon should be understood as a monsoon that is spatially extensive but of modest precipitation and that the collapse of the megamonsoon was because of the break-up of Pangaea and the movement of continents towards higher latitudes. In the Cretaceous, total continental area became much smaller, and fragmented continents were located at

middle and high latitudes, causing smaller land-monsoon area but heavier precipitation over small tropical continents. These results indicate that the modern global land monsoon did not directly originate from the Pangaea megamonsoon, but emerged after the reassembly of fragmented continents in the Cenozoic, and that continental configuration dominates the influence of greenhouse gas-induced temperature changes over geological time.

We compare our results with those from two independent sets of simulations performed for previous studies^{26,45}. Results from those simulations also show significant anticorrelations between land-monsoon area and precipitation, but with weaker correlation coefficients. The discrepancies are probably due to much lower resolutions of those models because precipitation is sensitive to model resolution⁴⁶.

Monsoon-related chemical weathering of silicate rocks has been shown to strongly influence atmospheric CO_2 concentration, consequently affecting global climate⁴⁷. Our simulations of the spatial and temporal evolution of land-monsoon area and intensity since Pangaea offer a broad perspective for further exploring the link between the global monsoon and Earth's climate history. The results also provide significant insights on the formation of exogenetic ore deposits that are strongly dependent on temperature and monsoon precipitation^{28,34}.

Our results demonstrate that regional monsoons have coherent spatial and temporal variations in tectonic timescales and that they are broadly consistent with the earlier findings about the Cenozoic Asian monsoon^{16,17} and African monsoons²². These results support the role of continental configuration as a primary control on the global monsoon system. Nevertheless, our study addresses only land-monsoon changes from a global perspective; linking this history with detailed regional monsoon evolution is not straightforward, partly because we use only a 10 Myr interval in our simulations and analyses. More detailed

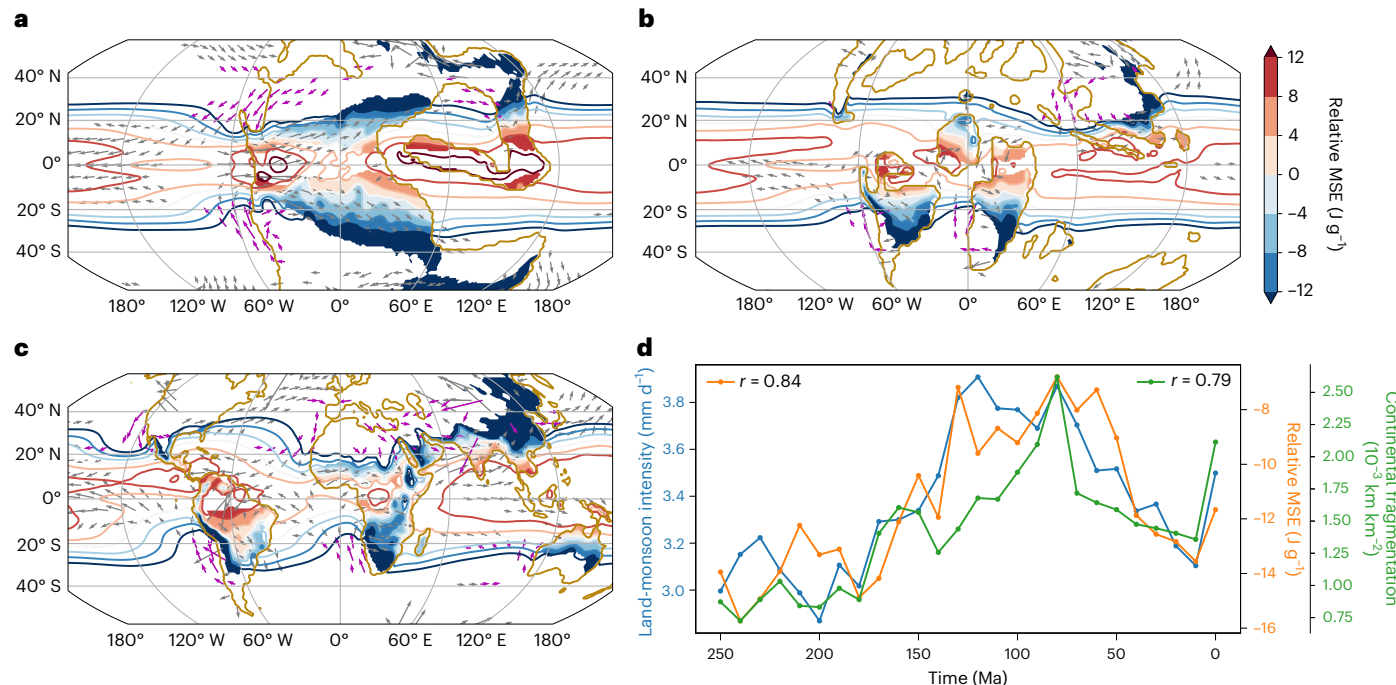


Fig. 4 | Circulation and energetics governing the evolution of land-monsoon intensity. **a–c**, Annual-mean relative MSE (contoured globally between -12 J g^{-1} and 12 J g^{-1} with an interval of 4 J g^{-1} , and shaded over the land-monsoon domain) and the zonally asymmetric 925 hPa horizontal wind (vectors are shown only where they exceed 3 m s^{-1} magnitude, and equatorward vectors in the subtropics ($20\text{--}45^\circ$ latitude) are coloured magenta) at 240 Ma (a), 80 Ma (b) and 0 Ma (c). Relative MSE, which is defined as the local surface air MSE minus the tropical-mean surface air MSE, provides a measure of convective instability. **d**, Time series

of land-monsoon intensity (blue line), the annual-mean relative MSE averaged over the land-monsoon domain (orange) and continental fragmentation (green). Land-monsoon intensity is the annual-mean precipitation amount horizontally averaged over the land-monsoon domain. Correlation coefficients between the simulated land-monsoon intensity and each other quantity are noted in the legend. Extended Data Fig. 5 repeats **a–c** for the boreal and austral summer seasons; the annual-mean relative MSE is used in this figure for simplicity and brevity.

geological evidence, including orographic and seaway histories, is also needed for addressing the evolution of regional monsoons^{14,15,17–27,48,49}.

Online content

Any methods, additional references, Nature Portfolio reporting summaries, source data, extended data, supplementary information, acknowledgements, peer review information; details of author contributions and competing interests; and statements of data and code availability are available at <https://doi.org/10.1038/s41561-023-01288-y>.

References

- Wang, B. & Ding, Q. Global monsoon: dominant mode of annual variation in the tropics. *Dyn. Atmos. Oceans* **44**, 165–183 (2008).
- Wang, P. et al. The global monsoon across time scales: mechanisms and outstanding issues. *Earth Sci. Rev.* **174**, 84–121 (2017).
- Geen, R., Bordoni, S., Battisti, D. S. & Hui, K. Monsoons, ITCZs and the concept of the global monsoon. *Rev. Geophys.* **58**, e2020RG000700 (2020).
- Mohtadi, M., Prange, M. & Steinke, S. Palaeoclimatic insights into forcing and response of monsoon rainfall. *Nature* **533**, 191–199 (2016).
- Neelin, J. in *The Global Circulation of the Atmosphere* (eds Schneider, T. & Sobel, A. H.) 267–301 (Princeton Univ. Press, 2007).
- Scotese, C. R. & Wright, N. PALEOMAP Paleodigital Elevation Models (PaleoDEMs) for the Phanerozoic (PALEOMAP Project, 2018); <https://www.earthbyte.org/paleodem-resource-scotese-and-wright-2018/>
- Wang, P. Global monsoon in a geological perspective. *Sci. Bull.* **54**, 1113–1136 (2009).
- Ramstein, G. et al. Some illustrations of large tectonically driven climate changes in Earth history. *Tectonics* **38**, 4454–4464 (2019).
- Robinson, P. L. in *Implications of Continental Drift to the Earth Sciences Vol. I* (eds Tarling, D. H. & Runcorn, S. K.) 449–476 (Academic Press, 1973).
- Kutzbach, J. & Gallimore, R. Pangaean climates: megamonsoons of the megacontinent. *J. Geophys. Res. Atmos.* **94**, 3341–3357 (1989).
- Parrish, J. T. Climate of the supercontinent Pangea. *J. Geol.* **101**, 215–233 (1993).
- Shields, C. A. & Kiehl, J. T. Monsoonal precipitation in the Paleo-Tethys warm pool during the latest Permian. *Palaeogeogr. Palaeoclimatol. Palaeoecol.* **491**, 123–136 (2018).
- Kutzbach, J., Guetter, P., Ruddiman, W. & Prell, W. Sensitivity of climate to late Cenozoic uplift in southern Asia and the American west: numerical experiments. *J. Geophys. Res. Atmos.* **94**, 18393–18407 (1989).
- Ruddiman, W. F. & Kutzbach, J. E. Forcing of late Cenozoic Northern Hemisphere climate by plateau uplift in southern Asia and the American West. *J. Geophys. Res. Atmos.* **94**, 18409–18427 (1989).
- Ramstein, G., Fluteau, F., Besse, J. & Joussaume, S. Effect of orogeny, plate motion and land-sea distribution on Eurasian climate change over the past 30 million years. *Nature* **386**, 788–795 (1997).
- Guo, Z. et al. Onset of Asian desertification by 22 Myr ago inferred from loess deposits in China. *Nature* **416**, 159–163 (2002).
- Liu, X. & Yin, Z.-Y. Sensitivity of East Asian monsoon climate to the uplift of the Tibetan Plateau. *Palaeogeogr. Palaeoclimatol. Palaeoecol.* **183**, 223–245 (2002).
- Sepulchre, P. et al. Tectonic uplift and eastern Africa aridification. *Science* **313**, 1419–1423 (2006).

19. Zhang, Z., Wang, H., Guo, Z. & Jiang, D. Impacts of tectonic changes on the reorganization of the Cenozoic paleoclimatic patterns in China. *Earth Planet. Sci. Lett.* **257**, 622–634 (2007).
20. Guo, Z. et al. A major reorganization of Asian climate by the early Miocene. *Clim. Past* **4**, 153–174 (2008).
21. Boos, W. R. & Kuang, Z. Dominant control of the South Asian monsoon by orographic insulation versus plateau heating. *Nature* **463**, 218–222 (2010).
22. Zhang, Z. et al. Aridification of the Sahara desert caused by Tethys Sea shrinkage during the late Miocene. *Nature* **513**, 401–404 (2014).
23. Licht, A. et al. Asian monsoons in a late Eocene greenhouse world. *Nature* **513**, 501–506 (2014).
24. Zhang, R. et al. Changes in Tibetan Plateau latitude as an important factor for understanding East Asian climate since the Eocene: a modeling study. *Earth Planet. Sci. Lett.* **484**, 295–308 (2018).
25. Zhu, C., Meng, J., Hu, Y., Wang, C. & Zhang, J. East-central Asian climate evolved with the northward migration of the high Proto-Tibetan Plateau. *Geophys. Res. Lett.* **46**, e8397–e8406 (2019).
26. Farnsworth, A. et al. Past East Asian monsoon evolution controlled by paleogeography, not CO₂. *Sci. Adv.* **5**, eaax1697 (2019).
27. Acosta, R. P., Ladant, J.-B., Zhu, J. & Poulsen, C. J. Evolution of the Atlantic Intertropical Convergence Zone, and the South American and African monsoons over the past 95-Myr and their impact on the tropical rainforests. *Paleoceanogr. Paleoclimatol.* **37**, e2021PA004383 (2022).
28. Parrish, J. T., Ziegler, A. & Scotese, C. R. Rainfall patterns and the distribution of coals and evaporites in the Mesozoic and Cenozoic. *Palaeogeogr. Palaeoclimatol. Palaeoecol.* **40**, 67–101 (1982).
29. Li, X. et al. A high-resolution climate simulation dataset for the past 540 million years. *Sci. Data* **9**, 371 (2022).
30. Li, X. et al. Climate variations in the past 250 million years and contributing factors. *Paleoceanogr. Paleoclimatol.* **38**, e2022PA004503 (2023).
31. Scotese, C. R. *Phanerozoic Temperature Curve (PALEOMAP Project, 2015)*; https://www.academia.edu/12114306/Phanerozoic_Global_Temperature_Curve
32. Scotese, C. R., Song, H., Mills, B. J. & vander Meer, D. G. Phanerozoic paleotemperatures: the Earth's changing climate during the last 540 million years. *Earth Sci. Rev.* **215**, 103503 (2021).
33. Rodwell, M. J. & Hoskins, B. J. Monsoons and the dynamics of deserts. *Q. J. R. Meteorol. Soc.* **122**, 1385–1404 (1996).
34. Bao, X. et al. Quantifying climate conditions for the formation of coals and evaporites. *Natl Sci. Rev.* <https://doi.org/10.1093/nsr/nwad051> (2023).
35. Ikeda, M. et al. Astronomical pacing of the global silica cycle recorded in Mesozoic bedded cherts. *Nat. Commun.* **8**, 15532 (2017).
36. Christensen, J. H. et al. in *Climate Change 2013: The Physical Science Basis* (eds Stocker, T. F. et al.) 1217–1308 (Cambridge Univ. Press, 2013).
37. Nie, J., Boos, W. R. & Kuang, Z. Observational evaluation of a convective quasi-equilibrium view of monsoons. *J. Clim.* **23**, 4416–4428 (2010).
38. Biasutti, M. et al. Global energetics and local physics as drivers of past, present and future monsoons. *Nat. Geosci.* **11**, 392–400 (2018).
39. Boos, W. R. & Korty, R. L. Regional energy budget control of the intertropical convergence zone and application to mid-Holocene rainfall. *Nat. Geosci.* **9**, 892–897 (2016).
40. Vecchi, G. A. & Soden, B. J. Increased tropical Atlantic wind shear in model projections of global warming. *Geophys. Res. Lett.* **34**, L08702 (2007).
41. Bombardi, R. J. & Boos, W. R. Explaining globally inhomogeneous future changes in monsoons using simple moist energy diagnostics. *J. Clim.* **34**, 8615–8634 (2021).
42. Chou, C., Neelin, J. D. & Su, H. Ocean-atmosphere-land feedbacks in an idealized monsoon. *Q. J. R. Meteorol. Soc.* **127**, 1869–1891 (2001).
43. Ditchek, S. D., Boos, W. R., Camargo, S. J. & Tippett, M. K. A genesis index for monsoon disturbances. *J. Clim.* **29**, 5189–5203 (2016).
44. Privé, N. C. & Plumb, R. A. Monsoon dynamics with interactive forcing. Part II: impact of eddies and asymmetric geometries. *J. Atmos. Sci.* **64**, 1431–1442 (2007).
45. Valdes, P. J., Scotese, C. R. & Lunt, D. J. Deep ocean temperatures through time. *Clim. Past* **17**, 1483–1506 (2021).
46. Demory, M.-E. et al. The role of horizontal resolution in simulating drivers of the global hydrological cycle. *Clim. Dyn.* **42**, 2201–2225 (2014).
47. Raymo, M. E. & Ruddiman, W. F. Tectonic forcing of late Cenozoic climate. *Nature* **359**, 117–122 (1992).
48. Boos, W. R. & Pascale, S. Mechanical forcing of the North American monsoon by orography. *Nature* **599**, 611–615 (2021).
49. Higuchi, T., Abe-Ouchi, A. & Chan, W.-L. Differences between present-day and Cretaceous hydrological cycle responses to rising CO₂ concentration. *Geophys. Res. Lett.* **48**, e2021GL094341 (2021).
50. Boucot, A. J., Xu, C., Scotese, C. R. & Morley, R. J. *Phanerozoic Paleoclimate: An Atlas of Lithologic Indicators of Climate* (SEPM, 2013).

Publisher's note Springer Nature remains neutral with regard to jurisdictional claims in published maps and institutional affiliations.

Springer Nature or its licensor (e.g. a society or other partner) holds exclusive rights to this article under a publishing agreement with the author(s) or other rightsholder(s); author self-archiving of the accepted manuscript version of this article is solely governed by the terms of such publishing agreement and applicable law.

© The Author(s), under exclusive licence to Springer Nature Limited 2023

Methods

Model and experiment designs

The model used in the present work is the Community Earth System Model version 1.2.2 (CESM1.2.2)⁵¹. Two steps of simulations are performed. For the first step, the lower-resolution version of the fully coupled atmosphere–ocean CESM1.2.2 ($3.75^\circ \times 3.75^\circ$ in latitude and longitude) is used to perform 26 slice simulations for the past 250 Myr, with a time interval of 10 Myr. In the simulations, palaeogeography is prescribed⁶. Solar constant is linearly increased from 98% at 250 Ma to 100% at present ($1,361 \text{ W m}^{-2}$) (ref. 52). Orbital parameters are all fixed at the present-day values. Atmospheric compositions are all the same as those of the pre-industrial values, except for CO₂.

Different from previous palaeoclimate simulation studies that used CO₂ reconstructions to constrain simulations, here we use reconstructed GMSTs^{31,32} to constrain our simulations. For each simulation, CO₂ concentration is tuned until the simulated GMST is asymptotic to the reconstructed GMST within 0.5°C (see Fig. 1a in refs. 29,30). All the simulations are integrated for more than 4,000 years to reach equilibrium states.

For the second step, sea surface temperatures in the lower-resolution simulations are used to drive the higher-resolution CESM atmosphere–land model ($0.9424^\circ \times 1.25^\circ$ in latitude and longitude). Palaeogeography, CO₂ concentrations and solar radiation remain the same as in the first step of simulations. Vegetation is prescribed, using that from the lower-resolution simulations. The higher-resolution simulations are integrated for 100 years. The results shown here are the averages over the past 60 years. Detailed information of the model and experiment set-up can be found in refs. 29,30.

We performed 26 sensitivity simulations to distinguish the role of palaeogeography from that of CO₂ concentrations and solar radiation in determining the global land monsoon. In these simulations, solar constant is fixed at the present-day value, CO₂ concentration is fixed at ten times the pre-industrial value (280 ppmv) and palaeogeography remains the same as that in the control simulations.

Global monsoon domains are defined with the global monsoon precipitation index^{1,2}. That is, monsoon domains are the regions where local summer-minus-winter precipitation exceeds 2 mm d^{-1} and local summer precipitation exceeds 55% of the annual total precipitation, and dry areas are defined as the local summer precipitation less than 1 mm d^{-1} . The local summer denotes May through September for the NH and November through March for the Southern Hemisphere, and local winter denotes November through March for the NH and May through September for the Southern Hemisphere.

To explicitly address how continental configurations impact global land-monsoon area and precipitation, we perform eight idealized simulations, using the lower-resolution coupled atmosphere–ocean CESM1.2.2. Four simulations are to test the impact of latitudinal locations of a supercontinent on land monsoons. An idealized supercontinent (A), with side lengths of 45° in latitude and 120° in longitude, is set at different latitudinal locations (Extended Data Fig. 5, left panels). The southern boundary of the supercontinent is at the Equator, 10°N , 20°N and 30°N , respectively. The other four simulations are to test the impact of continental area and fragmentation on land monsoons, in which the supercontinent in the previous four simulations is separated into three plates. Continent B has longitudinal length of 80° , and continents C and D have longitudinal length of 20° (Extended Data Fig. 5, right panels).

Definitions of continental fragmentation and mean latitude

To quantify the relationships between continental configurations and global land-monsoon area and precipitation, we define two extra parameters to characterize continental configurations, continental fragmentation and continental mean latitude, in addition to the continental area.

Continental fragmentation is defined as the ratio of the total length of continental coastlines to the total continental area. The

larger the ratio is, the more fragmented continents are. As shown in Extended Data Fig. 3d, the smallest continental fragmentation is about $0.7 \times 10^{-3} \text{ km km}^{-2}$ at 240 Ma. The largest fragmentation is about $2.6 \times 10^{-3} \text{ km km}^{-2}$ at 80 Ma. The averaged continental fragmentation of the Pangaea supercontinent (250–180 Ma) is about $0.9 \times 10^{-3} \text{ km km}^{-2}$. By contrast, the averaged fragmentation in the Cretaceous (130–80 Ma) is about $1.9 \times 10^{-3} \text{ km km}^{-2}$, twice as large as that of the Pangaea supercontinent.

The continental mean latitude is defined as the area-weighted mean latitude of all continents of both hemispheres. As shown in Extended Data Fig. 3c, the lowest mean latitude is about 35° at 220 Ma. The highest mean latitude is 41° at 100 Ma.

Energy-based index for monsoon area

We follow previous studies³⁹ and calculate the energy flux potential, χ , by taking the inverse Laplacian of the NEI to the atmosphere, which in turn is the sum of the surface sensible and latent heat fluxes and the net radiative flux into the top and bottom boundaries of the atmosphere, $\nabla^2 \chi = \text{NEI}$. The EFE is the zero line of the northward component of the divergent part of the vertically integrated atmospheric energy flux, \vec{v}_χ , where $\vec{v}_\chi = \nabla \chi$. Since tropical precipitation maxima generally move horizontally with the EFE and with χ minima³⁹, we create a diagnostic index for monsoon land area by summing the land area that falls within the lowest 7.5th percentile of χ during boreal and austral summer. The 7.5th percentile was chosen so that the value of this index averaged across all time-slice simulations matches land-monsoon area averaged across all simulations.

Uncertainties of coal and evaporite records

Coal and evaporite records have uncertainties of ages. They correspond to time intervals rather than exact times. The largest time interval of coal records is 38 Myr, the smallest interval is 5 Myr and the mean time interval of coals is 22 Myr. For evaporite records, the values are 44, 5 and 20 Myr, respectively. It would generate spatial and temporal uncertainties when these geological proxies are grouped to the 26 time slices³⁴.

Data availability

The data used in the present study are archived at

<https://doi.org/10.6084/m9.figshare.19920662.v1>.

References

1. Hurrell, J. W. et al. The Community Earth System Model: a framework for collaborative research. *Bull. Am. Meteorol. Soc.* **94**, 1339–1360 (2013).
2. Gough, D. O. Solar interior structure and luminosity variations. *Sol. Phys.* **74**, 21–34 (1981).

Acknowledgements

This work is supported by the National Natural Science Foundation of China, under grant 41888101. Simulations are conducted at the High-performance Computing Platform of Peking University.

Author contributions

Y.H. and Z.G. designed the research. X.L., J.G., J.L., Q.L., J.Z., S.Y., Q.W. and J.H. performed simulations. X.B. analysed proxy data of coals and evaporates. Y.H. and W.R.B. wrote the paper. All authors participated in analysis of results.

Competing interests

The authors declare no competing interests.

Additional information

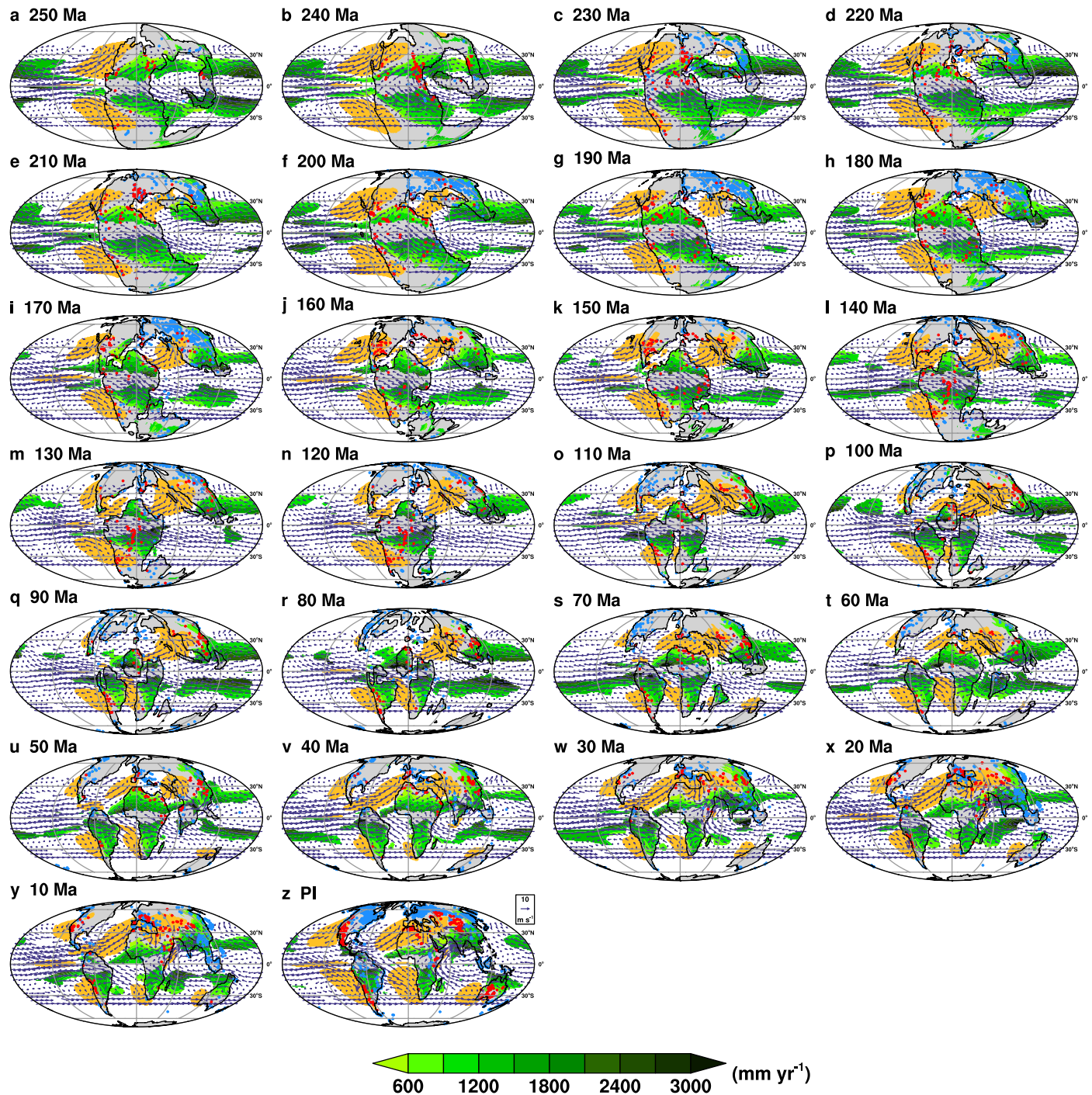
Extended data is available for this paper at <https://doi.org/10.1038/s41561-023-01288-y>.

Correspondence and requests for materials should be addressed to Yongyun Hu or Zhengtang Guo.

Peer review information *Nature Geoscience* thanks David McGee, Masayuki Ikeda and the other, anonymous, reviewer(s) for their

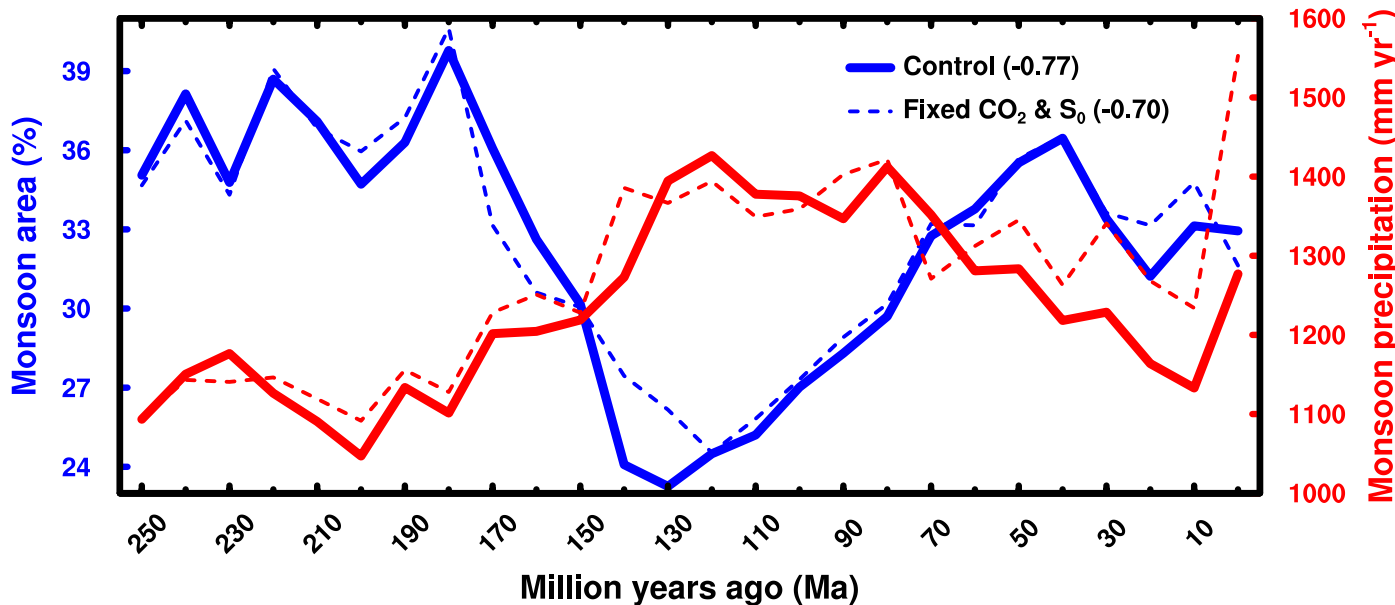
contribution to the peer review of this work. Primary Handling Editor: James Super, in collaboration with the *Nature Geoscience* team.

Reprints and permissions information is available at www.nature.com/reprints.



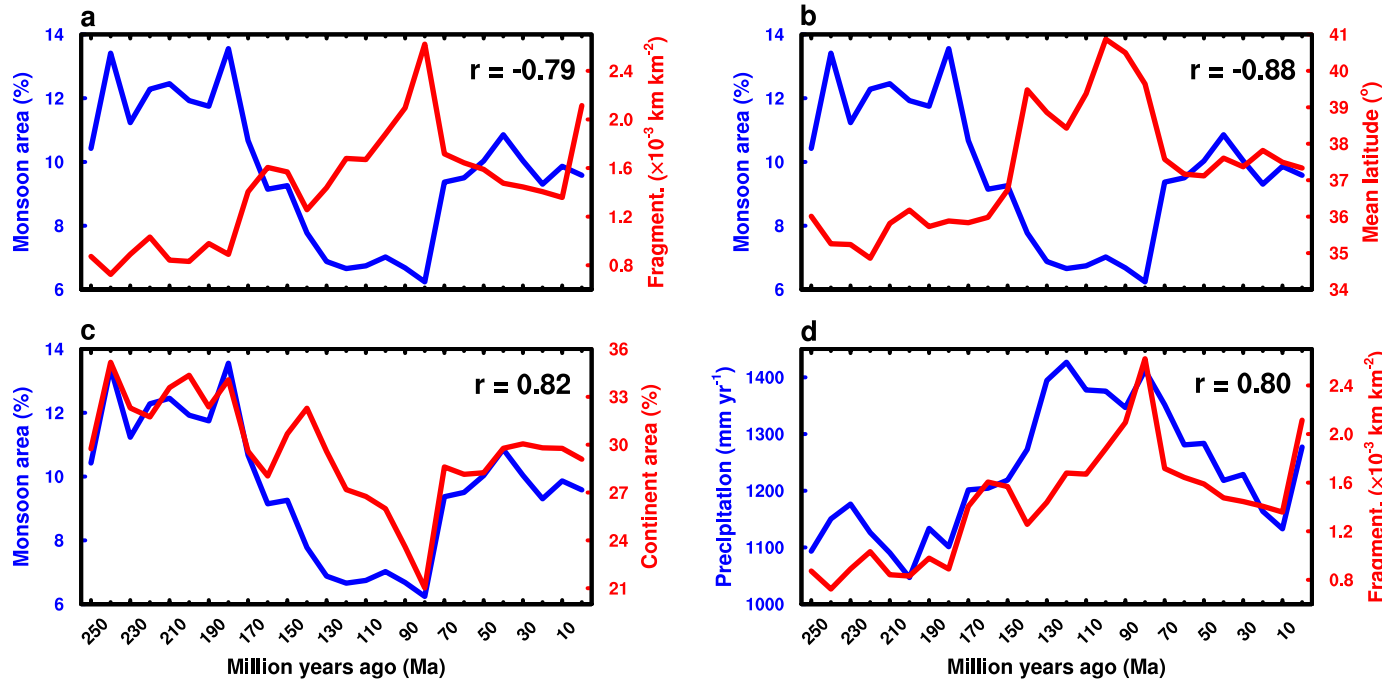
Extended Data Fig. 1 | Maps of global monsoon domains and annual-mean precipitation in 26 control simulations. Panels a–z present global monsoon domains and dry regions corresponding to the 26 control simulations. Global monsoon domains are defined with the monsoon precipitation index (MPI), and

the dry areas are defined as the local summer precipitation less than 1 mm yr⁻¹ (ref. 1,2). Monsoon domains are labeled with green, and dry areas are labeled with yellow. Arrows denote 850 hPa winds averaged over June-July-August (JJA). Blue and red dots denote coals and land-evaporites, respectively.



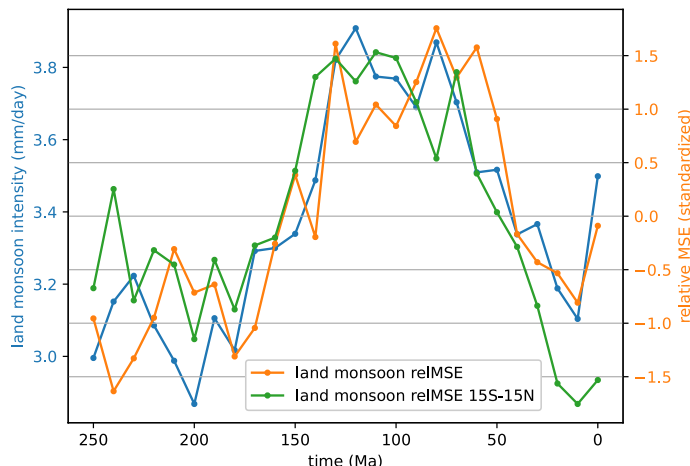
Extended Data Fig. 2 | Time series of global land-monsoon area and land-monsoon intensity. Solid lines are for control simulations, and thin dashed lines are for sensitivity simulations with fixed CO₂ concentration and solar constant.

Blue lines: global land-monsoon area as the percent of total continental area (left axis), and orange lines: annual-mean precipitation averaged over land-monsoon domains (right axis, mm yr⁻¹).



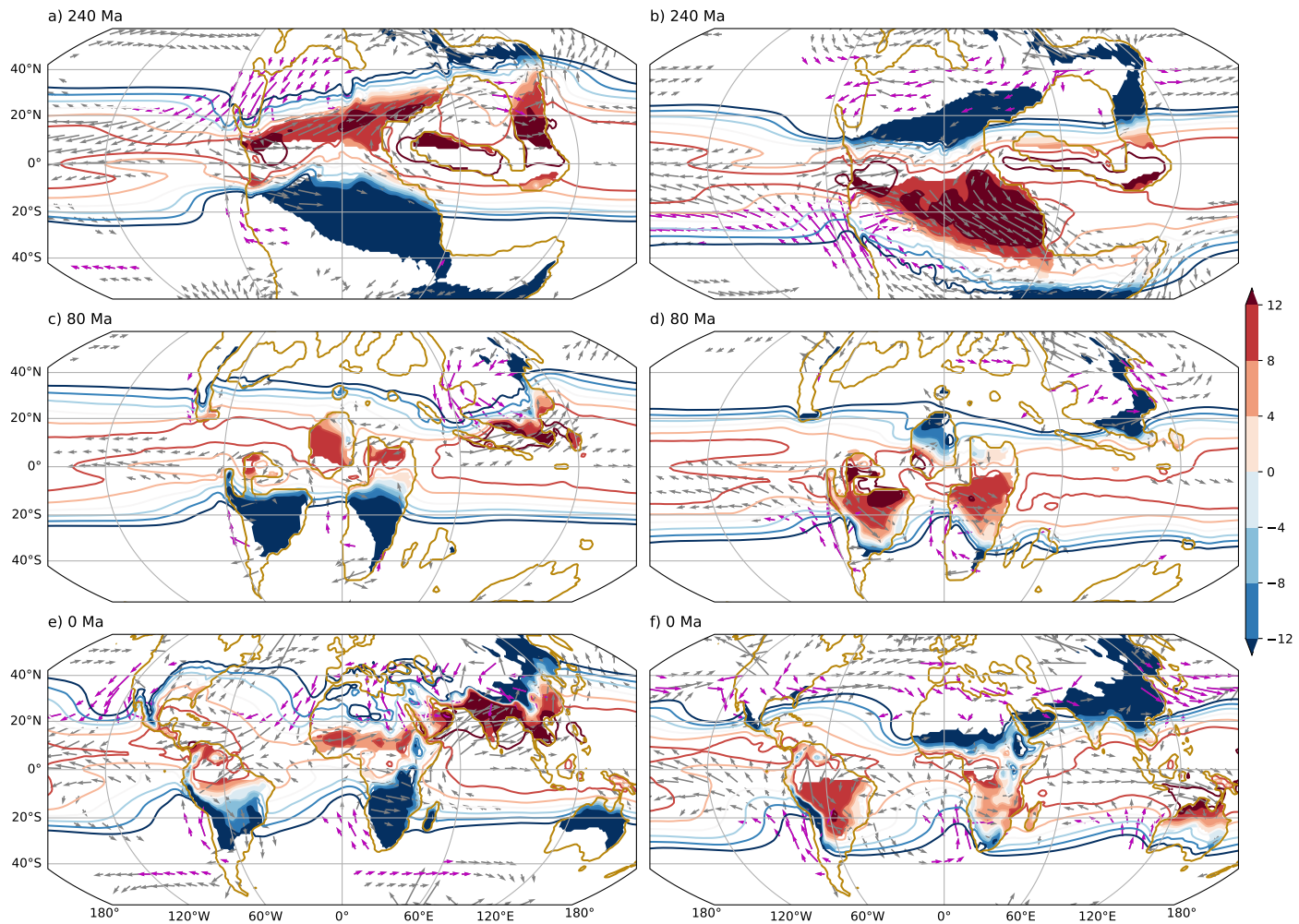
Extended Data Fig. 3 | Correlations of global land-monsoon area and precipitation with continental fragmentation, area, and mean-latitude.
a, Land-monsoon area with continental fragmentation; **b**, land-monsoon area with continental mean-latitude; **c**, land-monsoon area with total continental

area. The left vertical axis of plots a–c is the percentage of global land-monsoon area to Earth's surface area. **d**, Annual-mean land-monsoon precipitation with continental fragmentation.

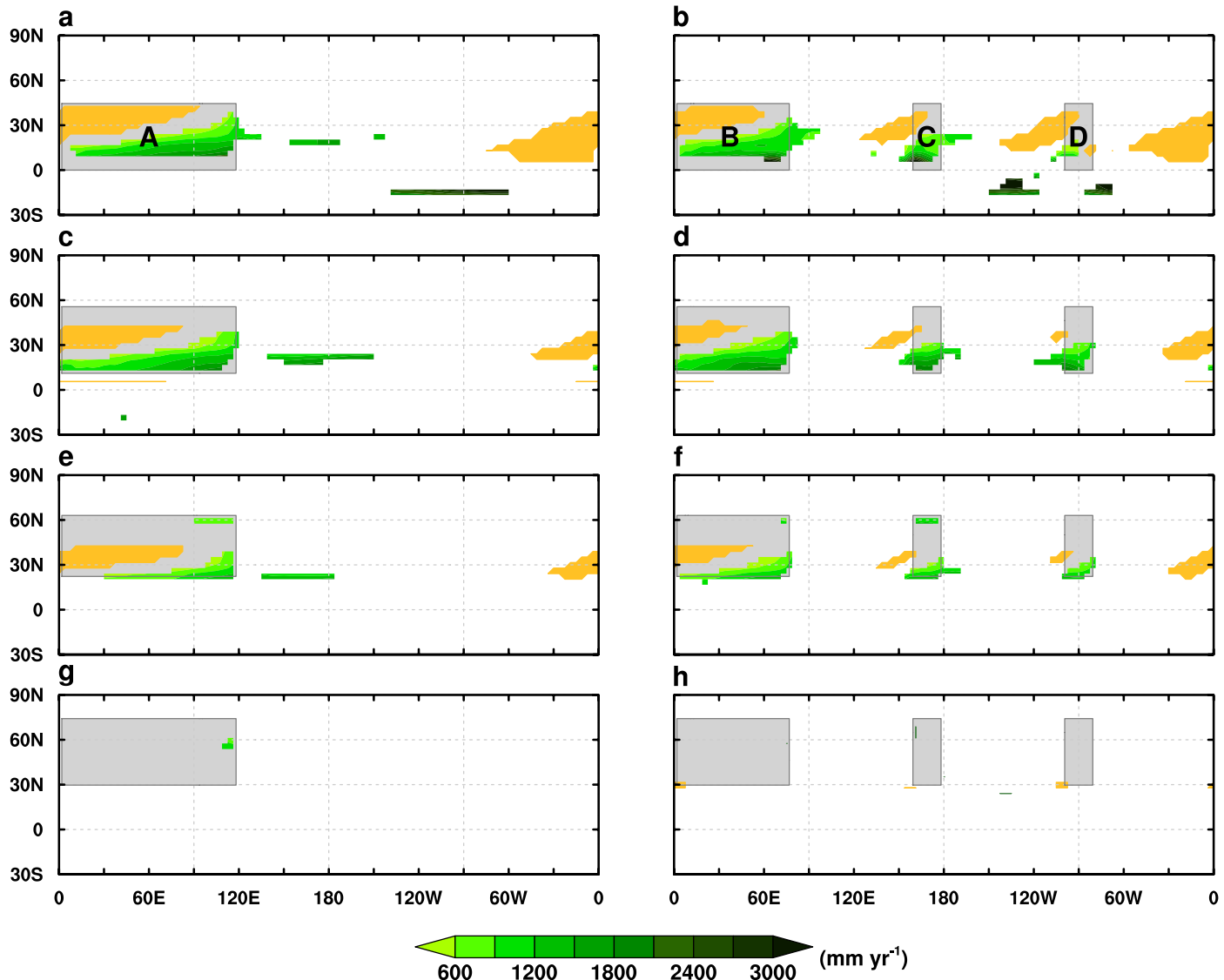


Extended Data Fig. 4 | Time series of land-monsoon precipitation intensity, relative MSE averaged over the land-monsoon domain, and relative MSE averaged over land-monsoon within 15° S – 15° N. The land monsoon intensity (blue line) is the same as in Fig. 4d. Relative MSE is shown averaged over the global

land-monsoon domain (orange) and only over the land-monsoon domain within 15° of the equator (green); both of these are standardized by subtracting their time-mean values and normalizing by their temporal standard deviation.

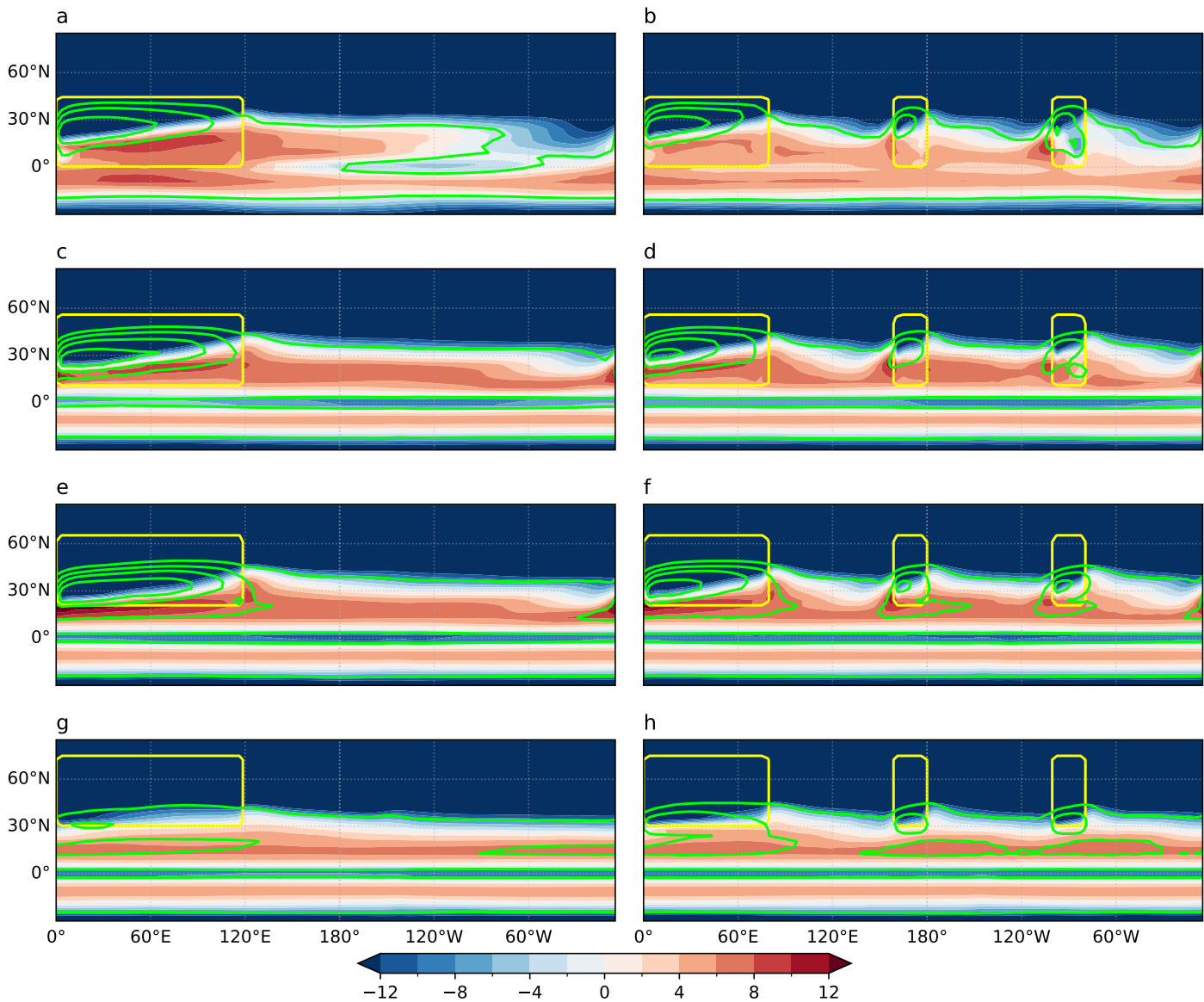


Extended Data Fig. 5 | Circulation and energetics governing the evolution of land-monsoon intensity. Same as Fig. 4a–c, except for boreal and austral summer-mean relative moist static energy (MSE). Left panels: boreal summer, and right panels: austral summer. From top to bottom, the panels correspond to 240 Ma, 80 Ma, and pre-industrial.

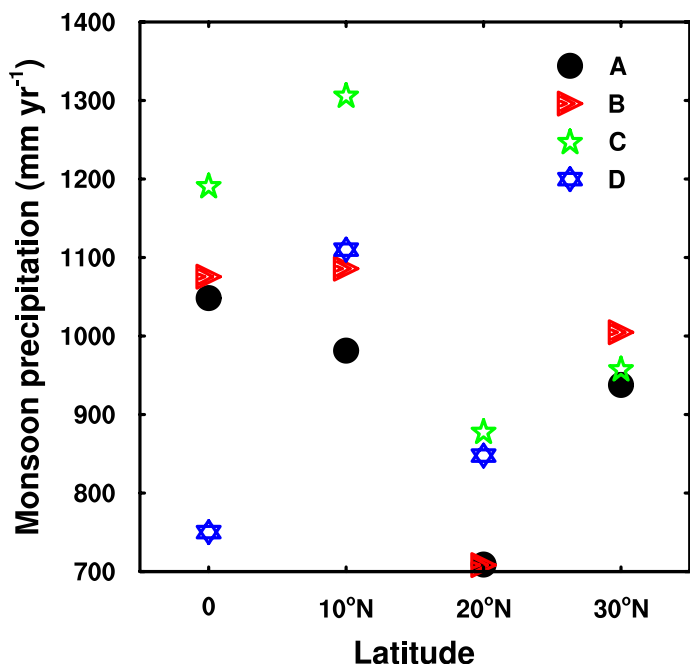


Extended Data Fig. 6 | Monsoon domains and annual-mean precipitation in idealized simulations for idealized continental configurations. Left panels, supercontinent A has side lengths of 45° in latitude and 120° in longitude. In the panels from top to bottom, the southern boundary of the supercontinent is set at the equator, 10 °N, 20 °N, and 30 °N, respectively. Right panels: same as left

panels, except that the supercontinent is separated into three plates. Continent B has a longitudinal length of 80°, and continents C and D have longitudinal length of 20°. Green colors denote monsoon domains, and yellow color denotes dry areas.



Extended Data Fig. 7 | Relative MSE for the idealized simulations. Color shading indicates relative MSE (inJ/g), orange contours denote surface temperatures, which start at 26°C with contour interval of 4°C . Continents are outlined in yellow, with geometries as described in Extended Data Fig. 6.



Extended Data Fig. 8 | Land-monsoon precipitation intensity in idealized simulations. Legends of continents are labeled in the upper-right corner of the plot.